Electrothermal Finite-Element Modeling for Defect Characterization in Thin-Film Silicon Solar Modules

Thomas Lanz, *Member, IEEE*, Mathias Bonmarin, *Member, IEEE*, Michael Stuckelberger, Christian Schlumpf, Christophe Ballif, and Beat Ruhstaller

***Abstract*—We present and validate a finite-element model for coupled charge and heat transport in monolithically interconnected thin-film solar modules. Using measured current–voltage (*I–V*) and lock-in thermography (LIT) measurements of amorphous silicon minimodules, we experimentally validate our model. The entire module volume is represented by two planes (front and back electrodes) which are coupled in vertical direction using 1-D models, leading to a large reduction of the degrees of freedom in the numerical model and contributing to an efficient solution approach. As compared to 3-D models, the vertical coupling of the charge transport is represented by local temperature-dependent *I–V* curves. These can be obtained by drift–diffusion calculations, single-cell measurements or, as presented here, by an analytical solar cell diode model. Inhomogeneous heat sources such as Joule's heating in the electrodes lead to nonuniform temperature distributions. The explicit temperature dependence in the local *I–V* curve, therefore, mediates the feedback of the thermal transport on the local electrical cell characteristics. We employ measured *I–V* curves under partial illumination and analytical solutions for the potential distribution to validate this approach. Further, with LIT measurements of the same modules with and without artificially induced electrical shunts, we verify the computed temperature distributions.**

***Index Terms*—Amorphous silicon, artificial shunt generation, characterization, defects, finite-element modeling (FEM), photovoltaic systems, simulation, thin-film devices.**

I. Introduction

WORLDWIDE installed photovoltaic capacity has undergone rapid growth over the past few years and solar electricity remains a very strong candidate for the large-scale deployment of renewable energy sources. Silicon thin-film solar cells and modules may be fabricated from abundant materials and are, therefore, viable for large-scale deployment [1]. Current developments include the tailoring of surface textures of transparent electrodes [2]–[4] and the associated processing steps [5]. Recently, dedicated manufacturing and modeling methods for the creation and tuning of diffractive and plasmonic structures have been proposed to increase the absorption in active layers [5]–[10]. Diminishing the conversion efficiency gap between current lab-scale solar cells and large-area solar modules necessitates a comprehensive understanding of the macroscopic device physics. Numerical modeling may assist in developing this understanding [11] and has attracted interest from device engineering. The characterization and design of electrical potential and temperature distributions in thin-film solar modules is an important task in view of nonideal operating conditions or defects such as partial shading, shunts, and local heat sources.

SPICE and its derivatives are well suited for the electrical characterization and optimization of solar modules. Typically representing the solar module by a network of equivalent circuit macromodels, it allows including the entire module area and quantitative electrical analyses [12]–[20]. While these approaches are able to reproduce measured current–voltage curves, they have some drawbacks: a refinement of the network—at a local defect for instance—requires a change in the network topology and not a mere refinement of the discretization. Furthermore, a current density distribution has to be mapped to a set of ideal resistors requiring a fine mesh to avoid changing the direction of the current. If thermal transport effects are to be considered, the thermal problem has to be translated into an additional equivalent electrical circuit, such that it can be solved by SPICE. The difficulty in mapping the simulation volume onto a network of discrete components in equivalent circuit modeling is circumvented in finite-element modeling (FEM) approaches, where the entire simulation domain may be represented by and discretized into smaller volumes [21], [22]. However, 3-D finite-element approaches are challenged by the large geometric aspect ratio found in thin-film solar modules. This necessitates a fine mesh leading to a large number of nodes and long computation times.

Experimentally, current–voltage (*I–V*) measurements and lock-in thermography (LIT) are commonly used for the characterization of solar cells and modules. LIT is a powerful tool in detecting and characterizing defects in solar cells and modules [20], [23], [24]. A physical model for the measured amplitude and phase information allows, e.g., extracting the local diode characteristics [25]. A quantitative understanding of the extracted temperature information requires a quantitative model for the charge and heat transport (coupled by Joule heat [26]) inside the solar cell or the module.

Manuscript received December 3, 2012; revised February 4, 2013; accepted February 21, 2013. Date of publication March 7, 2013; date of current version May 13, 2013. This work was supported by Swiss Electric Research under the Dursol project.

T. Lanz is with the Institute of Computational Physics, School of Engineering, Zurich University of Applied Sciences, CH-8401 Winterthur, Switzerland, and also with the Ecole Polytechnique Fédérale de Lausanne, 1015 Lausanne, Switzerland (e-mail: thomas.lanz@zhaw.ch).

M. Bonmarin and B. Ruhstaller are with the Institute of Computational Physics, School of Engineering, Zurich University of Applied Sciences, CH-8401 Winterthur, Switzerland (e-mail: mathias.bonmarin@zhaw.ch; beat.ruhstaller@zhaw.ch).

M. Stuckelberger, C. Schlumpf, and C. Ballif are with the Photovoltaics and Thin Film Electronics Laboratory, Institute of Microengineering, Ecole Polytechnique Fédérale de Lausanne, CH-2000 Neuchâtel, Switzerland (e-mail: michael.stuckelberger@epfl.ch; christian.schlumpf@epfl.ch; christophe.ballif@epfl.ch).

Color versions of one or more of the figures in this paper are available online at http://ieeexplore.ieee.org.

Digital Object Identifier 10.1109/JSTQE.2013.2250259

In this contribution, we present a new approach to the spatial modeling of the electrical and thermal transport in monolithically interconnected thin-film solar modules. Our model framework allows quantifying the detrimental effects that localized defects and small inhomogeneities have on the module level. Considering the very large aspect ratio of thin-film solar modules and their specific module topology, we project the volumes of the electrodes and active layers onto three distinct simulation domains, thus accounting for the entire module volume. This allows circumventing the aforementioned limitations for other simulation methods. This paper is organized as follows. Section II presents the numerical method and introduces the analytical and experimental means to validate it. Section III presents and discusses the experimental validation. Section IV concludes this paper.

II. Methods

A. Boundary-Value Problem for Thin-Film Modules

Careful convergence analyses such as in [17] emphasize that localized defects require a fine mesh to obtain accurate results. Concurrently, a fine mesh leads to large system equations and, therefore, requires efficient solvers. Our solution method is implemented in the finite-element multiphysics framework NM-SESES [27], [28], which allows the coupling of different physical fields and provides efficient numerics. NM-SESES computes the numerical solution of the equations of both electrical and thermal transport which, in our case, are coupled via Joule's heating and temperature-dependent local current–voltage curves. A Newton iteration scheme is used to obtain convergence for the coupled system. Our basic finite-element grid contains 48 960 nodes. On each node, we compute the electrical potential and the absolute temperature. Based on the constitutive material laws, we can then extract the charge and heat current distributions. The grid is predominantly rectangular except for the contacts of the artificial shunts where the grid is adjusted to the circular footprint of the solder points. The decomposition of the simulation volume into two parallel planes and a vertical coupling in between has already been applied to fuel cell modeling [29]. A sketch of the simulated thin-film minisolar module is presented in Fig. 1. We thus neglect the lateral charge transport in the amorphous silicon. This is justified, as the resistance of the amorphous silicon is by several orders of magnitude larger than the resistance of the ZnO. We restrict our numerical analysis to the steady state, i.e., we compute the equilibrated temperature and voltage distributions. The model may, thus, only be applied to measurements where a quasi-steady-state approximation is justified.

The electric transport in the plane electrodes is governed by the conservation of the current density $\mathbf{J}\left[\mathrm{A}\cdot\mathrm{m}^{-2}\right]$

$$\nabla\cdot\mathbf{J} = q_0 G \tag{1}$$

with $q_0 = 1.602\times10^{-19}\mathrm{C}$ the elementary charge and G the generation rate in $\left[\mathrm{s}^{-1}\cdot\mathrm{m}^{-3}\right]$. Using Ohm's law $\mathbf{J} = -\sigma\cdot\nabla\psi$, we obtain

$$-\nabla(\sigma\cdot\nabla\psi) = \frac{J_{1\mathrm{D}}}{d} \tag{2}$$

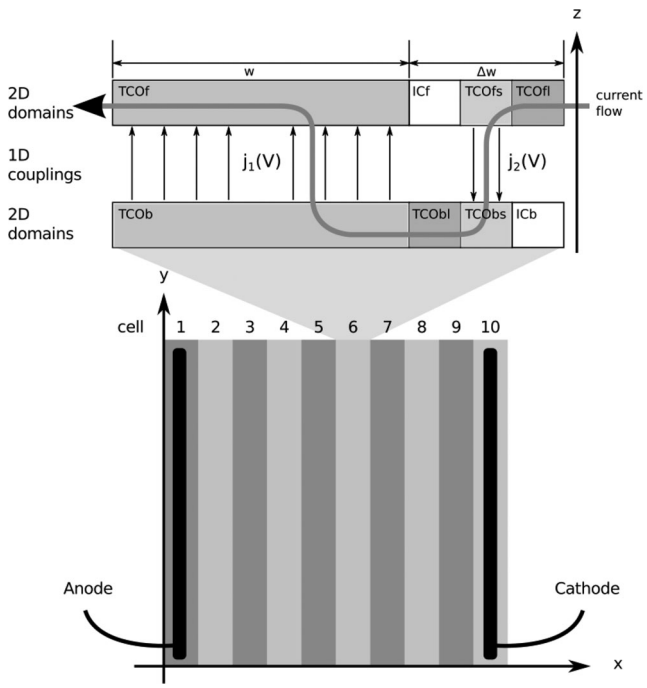

Fig. 1. Schematic illustration of the simulation domains used to represent the investigated thin-film minisolar module. The module consists of ten monolithically interconnected single junction cells with an area of 6.8 cm × 1 cm each. We refer to individual cells by their numbering as presented in the figure. External contacts are established on rear electrodes 1 and 10 with solder paste and aluminum stripes. Top: cross section of the unit cell of the two 2-D simulation domains representing the front and rear transparent conducting oxide (TCO) electrode. Note that these planes are perpendicular to the plane of the figure at bottom. The interconnection area is represented by six domains: TCO(f/b)(l/s) and IC(f/b), f and b denote front and back, l and s denote lateral and vertical, and IC interconnection, where no transport occurs. Bottom: layout of the bottom electrode and contacting scheme.

where $\sigma\left[\mathrm{S}\cdot\mathrm{m}^{-1}\right]$ is the conductivity, $\psi([\mathrm{V}])$ the electric potential, and $J_{1-\mathrm{D}}$ the current coupled in by the 1-D coupling. Assuming invariance in the vertical z-direction, this amounts to a source term $q_0 G = J_{1-\mathrm{D}}/d$, where $d\,[\mathrm{m}]$ is the thickness of the transparent electrode. As there is no dependence in z-direction, we may integrate the equation over the thickness of the electrode, which yields a factor of d and results in the 2-D formulation of the problem. We thus solve the equivalent problem of (2) multiplied by the thickness d and may write

$$\sigma_{2\mathrm{D}} = \sigma\cdot d = \frac{1}{R_{\mathrm{sheet}}} \tag{3}$$

as the sheet resistance $R_{\mathrm{sheet}}\left[\mathrm{S}^{-1}\right]$ is given by

$$R_{\mathrm{sheet}} = \frac{\rho}{d} = \frac{1}{\sigma\cdot d} \tag{4}$$

with $\rho\,[\mathrm{m/S}]$ being the resistivity. The electrical coupling between top and bottom electrode is given by a local *I–V* curve (see Fig. 1) parameterized as follows:

$$j_1(V) = j_0\left[\exp\left(\frac{q_0 V}{nkT}\right) - 1\right] - j_{\mathrm{photo}} + G_{\mathrm{shunt}} V\left(1 + b\left(1 - \frac{V}{V_{\mathrm{breakdown}}}\right)^{-m}\right) \tag{5}$$

with $n\,[1]$ being the ideality factor, $k = 1.381 \times 10^{-23}[\mathrm{J{\cdot}K^{-1}}]$ the Boltzmann constant, $T\,[\mathrm{K}]$ the temperature, $j_{\mathrm{photo}}\left[\mathrm{A{\cdot}m^{-2}}\right]$ the photocurrent, $G_{\mathrm{shunt}}\,[\mathrm{S}]$ the shunt conductance, and b, m (both $[1]$) and $V_{\mathrm{breakdown}}\,[\mathrm{V}]$ the breakdown parameters. The dark saturation current j_0 is given by [30]

$$j_0 = 1.5 \times 10^9 \exp\left(\frac{-E_g}{kT}\right) \text{in}\left[\mathrm{A{\cdot}m^{-2}}\right] \tag{6}$$

where $E_g\,[\mathrm{J}]$ is the bandgap energy. The above parameterization is our choice among many options that have been discussed in the literature (see, e.g., [1]) and we expect that our findings are largely robust against a change in this choice. In our parameterization, we allow for a linear shunt and a breakdown. The electrical coupling within the cell interconnection is ohmic and represented by an equivalent conductivity G_{equiv}

$$j_2(V) = G_{\mathrm{equiv}} V. \tag{7}$$

Similarly, for the thermal transport, we write

$$-\nabla(\kappa \cdot \nabla T) = q_{\mathrm{Joule}} - \sum_i \frac{F^i_{\mathrm{ext}}}{d} \tag{8}$$

where $\kappa\left[\mathrm{W{\cdot}m^{-1}{\cdot}K^{-1}}\right]$ is the thermal conductivity, $q_{\mathrm{Joule}}\left[\mathrm{W{\cdot}m^{-3}}\right]$ denotes the source term for Joule heating, and the external heat fluxes $F^i_{\mathrm{ext}}\left[\mathrm{W{\cdot}m^{-2}}\right]$ consist in convection, radiation transfer, parasitic absorption, and heat exchange between the upper and lower electrode. The coupling between the electrical and the thermal transport is given by Joule's heating

$$q_{\mathrm{Joule}} = \sigma|\nabla\psi|^2. \tag{9}$$

With Ohm's law

$$j = \sigma E = -\sigma\nabla\psi \tag{10}$$

where $E\left[\mathrm{V{\cdot}m^{-1}}\right]$ denotes the electric field, we obtain

$$q_{\mathrm{Joule}} = j \cdot E. \tag{11}$$

B. Analytical Solution and Validation of the FEM Approach

To validate our numerical approach and determine the required mesh density, we consider a case where we may derive the analytical expression for the potential distributions in the electrodes and the extracted current. To this end, we consider a single cell that is interconnected as in a module, as depicted in Fig. 1, however without the interconnection domains. We thus model the potential in domains *TCOf* and *TCOb*. We do not assume a homogeneous potential distribution in either the back or the front contact. The continuity equation for the current in the top electrode [see (1)] can be written as

$$\frac{\partial j_x}{\partial x} = \frac{j_{1\mathrm{D}}(x)}{d}. \tag{12}$$

We thus assume $j_y = 0$ due to the symmetry of the problem and $j_z = 0$, as we approximate the current density by transport in a plane. The generation is given by $G = j_{1\mathrm{D}}(x)/(q_0 d)$, where $j_{1\mathrm{D}}(x)$ is the local solar cell current and d the thickness of the electrode. In the bottom electrode, $j_{1\mathrm{D}}(x)$ appears as a sink. Using Ohm's law $\mathbf{J} = -\sigma \cdot \nabla\psi$, we obtain

$$\frac{\partial}{\partial x}\left(-\sigma\frac{\partial}{\partial x}\psi_T(x)\right) = \frac{j_{1\mathrm{D}}(x)}{d}. \tag{13}$$

To make our problem accessible to an analytical derivation, we linearize the local solar cell current according to

$$j_{1\mathrm{D}}(x) = j_{\mathrm{ph}} - \frac{\psi_T(x) - \psi_B(x)}{V_{\mathrm{oc}}} j_{\mathrm{ph}}. \tag{14}$$

We now substitute the dimension-less quantity $1/\theta^2 = j_{\mathrm{ph}}/(\sigma d V_{\mathrm{oc}})$ whereby we assume an isotropic conductivity. We now state the system of equations with boundary conditions:

$$-\frac{\partial^2}{\partial x^2}\psi_T(x) = \frac{V_{\mathrm{oc}} - (\psi_T(x) - \psi_B(x))}{\theta^2} \tag{15}$$

$$-\frac{\partial^2}{\partial x^2}\psi_B(x) = -\frac{V_{\mathrm{oc}} - (\psi_T(x) - \psi_B(x))}{\theta^2} \tag{16}$$

$$\psi_T\left(-L/2\right) = V_{\mathrm{app}}/2 \quad \psi_B\left(L/2\right) = -V_{\mathrm{app}}/2 \tag{17}$$

$$\frac{\partial\psi_T\left(L/2\right)}{\partial x} = 0 \quad \frac{\partial\psi_B\left(-L/2\right)}{\partial x} = 0. \tag{18}$$

We have now obtained an inhomogeneous system of linear differential equations of second order. For a given potential distribution, the extracted current is implicitly given by Ohm's law:

$$J(V_{\mathrm{app}}) = -\sigma\frac{\partial\psi_T\left(-L/2\right)}{\partial x}. \tag{19}$$

We note that one trivial particular solution for the potential distributions is given for $V_{\mathrm{app}} = V_{\mathrm{oc}}$ by $\psi_T\left(x\right) \equiv -\psi_B\left(x\right) \equiv V_{\mathrm{oc}}/2$.

We now turn to calculate the error between the analytical and the numerical solution. For this, we consider the nontrivial case $V_{\mathrm{app}} = V_{\mathrm{oc}}/2 = 1/2$ V. For simplicity and without loss of generality, we set $L = j_{\mathrm{ph}} = d = \sigma = 1$, and therefore, $\theta = 1$. For these constants and boundary conditions, the solution is given by

$$\psi_T(x) = \frac{1}{2}\left(\frac{\sqrt{2}x\sinh\left(\frac{1}{\sqrt{2}}\right) - \cosh\left(\sqrt{2}x\right)}{\sqrt{2}\sinh\left(\frac{1}{\sqrt{2}}\right) + 2\cosh\left(\frac{1}{\sqrt{2}}\right)} + 1\right) \tag{20}$$

$$\psi_B(x) = \frac{1}{2}\left(\frac{\sqrt{2}x\sinh\left(\frac{1}{\sqrt{2}}\right) + \cosh\left(\sqrt{2}x\right)}{\sqrt{2}\sinh\left(\frac{1}{\sqrt{2}}\right) + 2\cosh\left(\frac{1}{\sqrt{2}}\right)} - 1\right) \tag{21}$$

$$J(V_{\mathrm{oc}}/2) = -\frac{1}{1 + \sqrt{2}\coth\left(\frac{1}{\sqrt{2}}\right)} \approx 0.3\ \mathrm{A}. \tag{22}$$

In Fig. 2, we plot the solution for the top $(\psi_T(x))$ and the bottom $(\psi_B(x))$ contact. The numerical accuracy of the solution increases by refining the mesh, as illustrated in Fig. 3, where we plot the numerical error as a function of the number of nodes that we use to discretize the simulation domain. Note that we determine the error between the analytical and the numerical solutions of the potential distributions, and the external current [see (20)–(22)]. As the external current is implicitly determined by the potential distribution, we obtain the same convergence rate as for the potential.

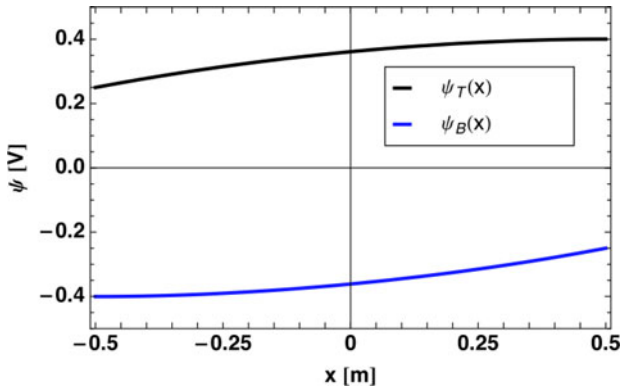

Fig. 2. Analytical solution of the potential distribution in the top and bottom electrode for $V_{\rm app} = V_{\rm oc}/2$, $L = 1$, and $\theta = 1$.

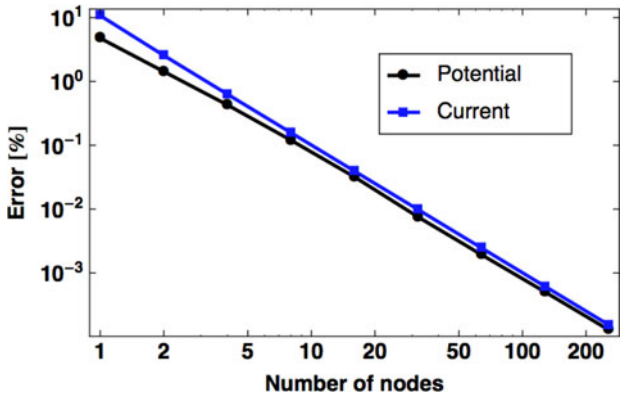

Fig. 3. Numerical error in the computed potential distribution and extracted current through the top electrode as a function of the number of nodes for $V_{\rm app} = V_{\rm oc}/2$, $L = 1$, and $\theta = 1$.

TABLE I
ELECTRICAL CELL PARAMETERS EXTRACTED FROM THE CURRENT–VOLTAGE MEASUREMENTS UNDER FULL AND PARTIALLY SHADED AM1.5 ILLUMINATION

Parameter	Value [Unit]	Parameter	Value [Unit]
j_0 at 300 K	$2.87 \cdot 10^{-2}$ A/m^2	q/(n k)	3660 K / V
$j_{\rm photo}$	116.8 A/m^2	$G_{\rm shunts}$	5.20 S
b	1 %	$V_{\rm breakdown}$	−2.5 V
m	−8 (1)		

C. Experimental Methods

1) Amorphous Silicon Minisolar Modules: For the experimental verification of our modeling results, we use amorphous silicon minimodules that are cut out of an industrial size module. The modules were produced in an industrial reactor; however, no back reflector or encapsulation was realized. This allows for direct access to the rear electrode. Both front and back electrode materials are low-pressure chemical vapor deposition ZnO. The active cell consists of a p-i-n superstrate structure, which is deposited on the ZnO-Glass substrate. The module contains ten cells (of which only cells 2–10 are connected) with an area of 6.8 cm × 1 cm each. Contacts on the modules are established using solder paste on the rear electrodes of the first and the last serially connected cell; the last cell, cell 1, is thus isolated. Therefore, only cells 2–10 remain active.

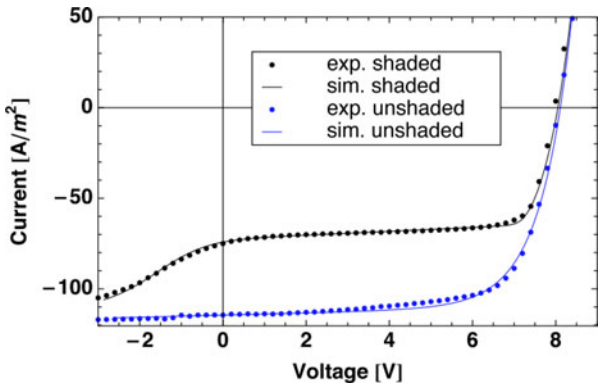

Fig. 4. Numerical solution and measured *I–V* curves for a-Si minimodule with shading.

2) Current–Voltage Curves Under Partial Illumination: Current–voltage curves are obtained under AM1.5 illumination (Wacom 4-source sun simulator, AAA rating) with a controlled voltage source (Keithley 2601A). Shading was realized using wire mesh equal density filters with a transmission of $T = 58\%$. Artificial shunts were realized using aluminum stripes that we soldered onto the accessible back contacts.

3) Lock-in-Thermography: In this study, an experimental LIT setup has been custom designed in our laboratory in Winterthur, Switzerland. The solar cell contacts are connected to an ac/dc power supply (VSP 1410, Voltcraft). The cover glass is directly sucked to a thick metallic heat sink. A highly sensitive microbolometer camera (PI450, Optris GmbH) synchronized with the voltage modulation signal records the thermal emission of the solar cell surface. Thermal images are recorded with the camera facing the rear transparent electrode. The infrared images are demodulated by a computer according to the standard lock-in method (SLIM [23]). The amplitude and phase images resulting from this demodulation are displayed in pseudocolors. The ac modulation frequency is chosen high enough to ensure a proper rejection of the signal dc part, and it compensates for the lateral heat spreading. The number of modulation cycles is chosen to achieve the desired sensitivity S (in Kelvins) [23]:

$$S = \frac{\text{NETD}}{\sqrt{\text{frame rate} \times t_{\rm acquisition}}}. \tag{23}$$

In our case, the noise equivalent temperature difference NETD = 40 mK, frame rate = 80 Hz, and $t_{\rm acquisition} = 150$ s. The temperature sensitivity in our setup, thus, amounts to $S \approx 0.4$ mK, and we thus scale the obtained lock-in amplitude to this value.

III. RESULTS AND EXPERIMENTAL VALIDATION

A. Electrical Model: Partially Shaded Amorphous Silicon Minimodules

In Fig. 4, we present the current–voltage measurements of the studied amorphous silicon solar minimodule under full and

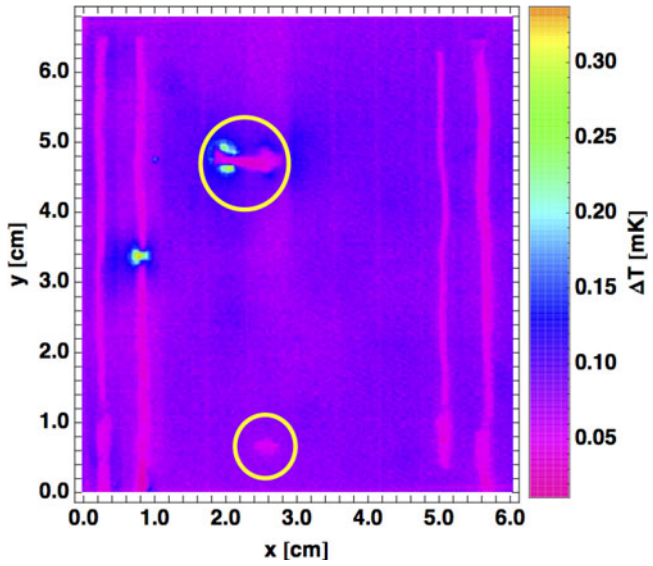

Fig. 5. Reverse bias dark lock-in amplitude image of the amorphous silicon minimodule measured at -4 V dc and scaled to 0.35 mK. AC modulation amplitude is 8 V, modulation frequency is 1 Hz, and integration over 150 periods.

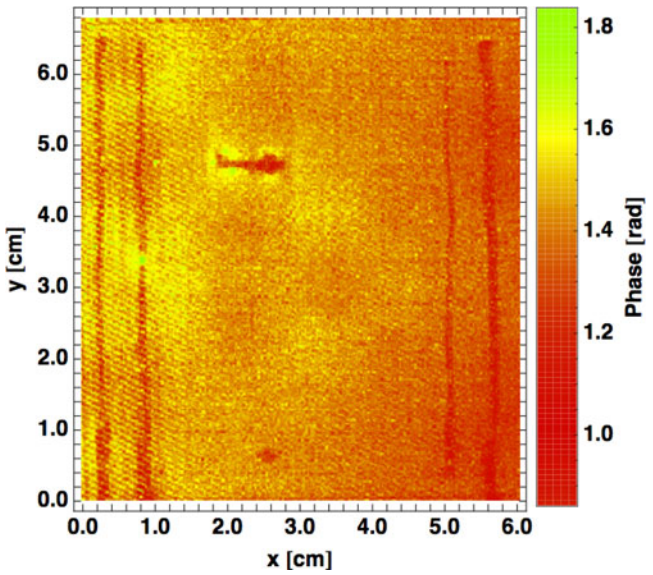

Fig. 6. Reverse bias dark lock-in phase image of the amorphous silicon minimodule measured at -4 V dc. The phase image corresponds to the wavefronts of the temperature response of the module. Experimental parameters identical to Fig. 5.

partially shaded AM1.5 illumination. The blue-dotted line shows the current–voltage curve as measured under standard test conditions, i.e., revealing photocurrent, fill factor, and open-circuit voltage of the module. The blue solid line shows our model calculation, accurately reproducing the measured curve. The upper black-dotted line shows the *I*–*V* measurement under partial illumination: we shade cell number 10 (for cell numbering, see Fig. 1) using an equal density wire mesh filter with a partial transmission of $T = 58\%$. We simulate this measurement (black solid line) by scaling the photocurrent of the shaded cell by 58%. As is apparent in Fig. 4, the shaded cell is operated at reverse and its reverse characteristic is revealed in the $(-2, 1)$ voltage range producing the well-known S-shaped voltage curve of modules containing shaded or shunted cells. The numerical model also accurately reproduces the measurement under partial illumination. In principle, the analysis for such a well-defined shading pattern can also be done analytically (see, e.g., [1]), and hence, we expect to obtain a quantitative agreement. Given our model simplifications, such as the parameterization of the 1-D coupling, the numerical correspondence and accuracy between experiment and simulation will be harder to obtain for more complicated shading patterns.

B. Electrothermally Coupled Model: Shunts and Inhomogeneous Conductivity

Partially shading an entire cell is a well-controllable experiment and does not require a spatial charge transport model. The above result of Section III-A could also be achieved with a simple equivalent circuit model containing macromodels for each cell. To motivate and validate our multiphysics spatial model, we now turn to the case of localized defects. To this end, we introduce two artificial defects in the minimodule, as can be seen in Fig. 5 (experimental details below).

To validate the thermal transport model in the solar module model, we use LIT measurements as described previously. As we intend to simulate the measurement with a steady-state model, we choose a low excitation frequency of 1 Hz. As the studied minimodule contained no severe shunts, we introduced two artificial defects. First, a short aluminum stripe was soldered to the back contacts of two neighboring cells, creating a short circuit. Second, again using solder paste, we created a small patch of solder paste on the back contact of cell number 5 (cf., Fig. 1), thus changing the local effective sheet conductivity of the back contact. We chose to introduce the shunts in this way to obtain defects that can be implemented straightforwardly in the model (for other possibilities, see, e.g., [11] and [20]). We positioned the defects to avoid a symmetrical configuration; otherwise, we did not study in detail the specific influence of the shunt position (cf., e.g., [19]). Both defects are clearly visible in the LIT measurements, in both amplitude, as presented in Fig. 5 (where we have highlighted the defects with yellow circles) and in phase, as presented in Fig. 6. The bright spot on cell 2 on the left in Fig. 5 is a result of the manually applied silver paste whose width narrows at this spot and was not considered in the FEM model. Representing these engineered defects in our numerical model of the solar module again requires a projection onto the simulation domains. We effectively model both defects by a locally increased electrical and thermal conductivity of the rear simulation plane representing the back electrode and, within the domains of the shunts, the solder paste. As the lower simulation domain represents the entire device volume below the absorber layer, the model equations are formulated in terms of effective or sheet conductivities, as discussed in (4).

The numerical results are presented in Figs. 7 and 8. In the model, we include the two outer solder stripes that establish the external contacts and the two soldered defects that are

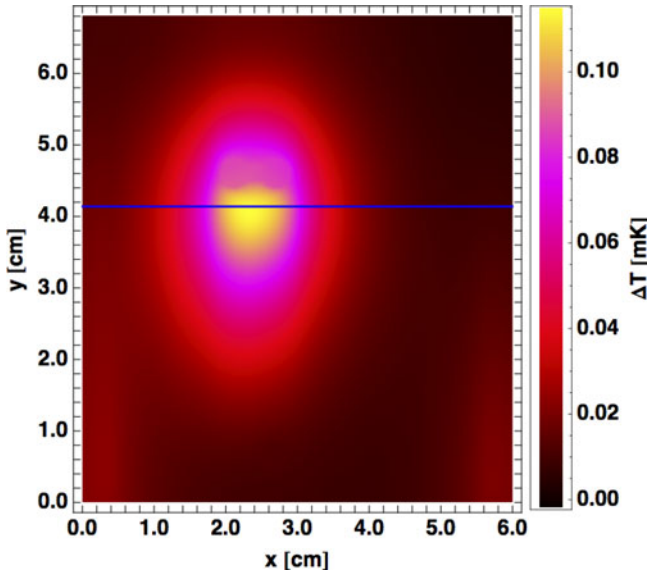

Fig. 7. Calculated steady-state temperature distribution for $V_{\rm app} = -4$ V. Geometry and model parameters in Fig. 1 and Table I. In Fig. 9, we plot the computed electrical potential distribution along the blue line in the figure.

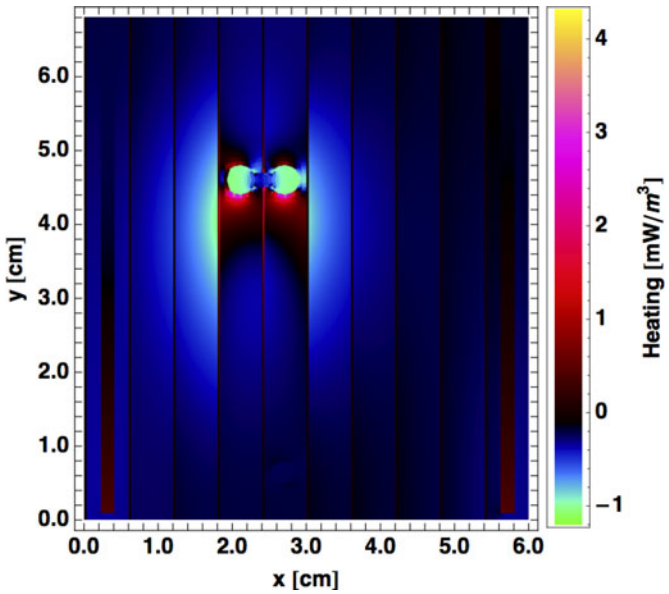

Fig. 8. Calculated steady-state heating distribution for $V_{\rm app} = -4$ V. Geometry and model parameters in Fig. 1 and Table I.

highlighted in Fig. 5. Our model—so far—solves for the stationary solution of the equations for a constant voltage bias. The thus obtained temperature distribution is presented in Fig. 7. The increased local temperature in the vicinity of the shunt across the cell boundary is clearly visible. Furthermore, this temperature increase, around 0.1 mK, is in the same order of magnitude as the measured temperature increase; cf., Fig. 5, where we obtain around 0.3 mK. LIT reveals the shunt-induced heating [23]. Our numerical model also computes the local heat divergence, or heating [cf., right side of (8)].

In Fig. 8, we present this numerically determined heating distribution which, just as in the electrical case, is deduced from

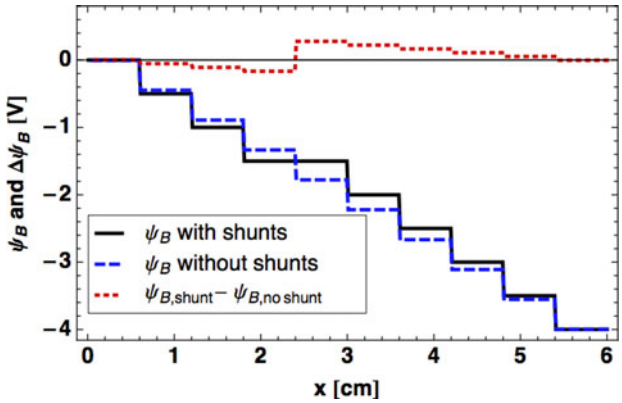

Fig. 9. Plot of the computed steady-state electrical potential distribution across all stripes in the back contact for $V_{\rm app} = -4$ V along the line $[x = 0 - 6$ cm, $y = 4.2$ cm] (cf., Fig. 7), similar as in Fig. 2. Solid black line: with shunts as described in the text, dashed blue line: without shunts, dotted red line: $\psi_{\rm B,with\ shunts}(x) - \psi_{\rm B,no\ shunts}(x)$.

the temperature distribution and the associated material laws. Close inspection of Fig. 8 reveals the influence of both soldered defects on the heating distribution. On the bottom of Fig. 8, the solder point appears slightly brighter as its local neighborhood. On the top of Fig. 8, the immediate vicinity of the short circuit is shown to be heated by a large current that flows between the two back contacts. The shunt across the cell boundary itself acts as a heat dissipator with a corresponding negative heating rate. To illustrate the extended effect of the shunts, we plot in Fig. 9 the computed electrical potential distribution along the line $[x = 0 - 6$ cm, $y = 4.2$ cm], similar as in Fig. 2.

IV. Discussion and Conclusion

We have presented our recently developed FEM of the spatial electrical and thermal transport in thin-film solar modules. This model has been validated on the example of an amorphous silicon solar minimodule that consists of nine monolithically interconnected solar cells. Using current–voltage measurements with and without partial shading and LIT measurements in the dark, we experimentally characterize the detrimental effects of artificially created shunts that are electrically and thermally active. Using our numerical model, we successfully reproduce the measured *I–V* curves. Further, the model qualitatively correctly accounts for the thermal signal of shunts obtained by LIT in the dark.

Our numerical results and their comparison with experimental data support our claim of correctly including the relevant physics for the coupled problem of electrothermal transport in defect-affected thin-film solar modules. Furthermore, having both electrical potential and temperature distribution at hand allows for advanced investigations such as computing the locally produced or dissipated power. This may be used to quantitatively characterize the detrimental nonlocal effect of inhomogeneous conductivities and localized shunts. So far, we cannot, however, reproduce the experimentally obtained amplitude and phase information that we get from LIT. This will be possible once we solve the time-resolved equations with ac bias. We now

intend to use our model for the analysis and characterization of degradation phenomena in thin-film solar modules. Thanks to the underlying efficient numerical framework, the model-based study of the detrimental long-term effects of nonuniform layer thicknesses and water ingress, e.g., is within reach using our model.

ACKNOWLEDGMENT

The authors would like to thank G. Sartoris and E. Knapp of the Institute of Computational Physics, Zurich University of Applied Sciences (ZHAW), Winterthur, Switzerland, for fruitful discussions and valuable advice in setting up the model; M. Bonnet-Eymard of the Institute of Microtechnology, Ecole Polytechnique Fédérale de Lausanne, Neuchâtel, Switzerland for assistance with the *I–V* measurements; and F. Baumgartner and D. Schär of the Institute of Energy Systems and Fluid Engineering, ZHAW, for helpful advice on solar module technology. They further thank Winterthur Instruments AG for providing the microbolometer camera used in this study.

REFERENCES

[1] A. V. Shah, *Thin-Film Silicon Solar Cells,* A. V. Shah, Ed. Lausanne, Switzerland: EPFL Press, 2010.

[2] M. Boccard, T. Soderstrom, P. Cuony, C. Battaglia, S. Hänni, S. Nicolay, L. Ding, M. Benkhaira, G. Bugnon, A. Billet, M. Charrière, F. Meillaud, M. Despeisse, and C. Ballif, "Optimization of ZnO front electrodes for high-efficiency micromorph thin-film Si solar cells," *IEEE J. Photovoltaic*, vol. 2, no. 3, pp. 229–235, Jul. 2012.

[3] L. Ding, M. Boccard, G. Bugnon, M. Benkhaira, M. Despeisse, F. Sculati-Meillaud, S. Nicolay, P. Losio, O. Kluth, P. Carroy, O. Caglar, and C. Ballif, "New generation transparent LPCVD ZnO electrodes for enhanced photocurrent in micromorph solar cells and modules," *IEEE J. Photovoltaic*, vol. 2, no. 2, pp. 88–93, Apr. 2012.

[4] M. Boccard, P. Cuony, C. Battaglia, S. Hänni, S. Nicolay, L. Ding, M. Benkhaira, G. Bugnon, A. Billet, M. Charriére, K. Soderstrom, J. Escarré and, F. Sculati-Meillaud, M. Despeisse, and C. Ballif, "Nanometer- and micrometer-scale texturing for high-efficiency micromorph thin-film silicon solar cells," *IEEE J. Photovoltaic*, vol. 2, no. 2, pp. 83–87, Apr. 2012.

[5] C. Battaglia, J. Escarré, K. Söderström, L. Erni, L. Ding, G. Bugnon, A. Billet, M. Boccard, L. Barraud, S. De Wolf, F.-J. Haug, M. Despeisse, and C. Ballif, "Nanoimprint lithography for high-efficiency thin-film silicon solar cells," *Nano Lett.*, vol. 11, no. 2, pp. 661–665, 2011.

[6] T. Lanz, B. Ruhstaller, C. Battaglia, and C. Ballif, "Extended light scattering model incorporating coherence for thin-film silicon solar cells," *J. Appl. Phys.*, vol. 110, no. 3, pp. 033111-1–033111-6, 2011.

[7] T. Lanz, L. Fang, S. Baik, K. Lim, and B. Ruhstaller, "Photocurrent increase in amorphous Si solar cells by increased reflectivity of LiF/Al electrodes," *Solar Energ. Mater. Solar Cells*, vol. 107, pp. 259–262, 2012.

[8] J. Grandidier, R. A. Weitekamp, M. G. Deceglie, D. M. Callahan, C. Battaglia, C. R. Bukowsky, C. Ballif, R. H. Grubbs, and H. A. Atwater. (2012). Solar cell efficiency enhancement via light trapping in printable resonant dielectric nanosphere arrays. *Phys. Status Solidi (a)*, [Online]. Available: http://dx.doi.org/10.1002/pssa.201228690

[9] A. Bozzola, M. Liscidini, and L. C. Andreani, "Photonic light-trapping versus Lambertian limits in thin film silicon solar cells with 1D and 2D periodic patterns," *Opt. Exp.*, vol. 20, no. S2, pp. A224–A244, Mar. 2012.

[10] P. Kowalczewski, M. Liscidini, and L. C. Andreani, "Engineering gaussian disorder at rough interfaces for light trapping in thin-film solar cells," *Opt. Lett.*, vol. 37, no. 23, pp. 4868–4870, Dec. 2012.

[11] S. Vergura, G. Acciani, and O. Falcone, "A finite-element approach to analyze the thermal effect of defects on silicon-based PV cells," *IEEE Trans. Ind. Electron.*, vol. 59, no. 10, pp. 3860–3867, Oct. 2012.

[12] M. Steiner, G. Siefer, and A. W. Bett. (2012). An investigation of solar cell interconnection schemes within cpv modules using a validated temperature-dependent spice network model. *Progr. Photovol. Res. Appl.*, [Online]. Available: http://dx.doi.org/10.1002/pip.2284

[13] K. Brecl and M. Topič, "Simulation of losses in thin-film silicon modules for different configurations and front contacts," *Progr. Photovoltaic Res. Appl.*, vol. 16, no. 6, pp. 479–488, 2008.

[14] K. Brecl, M. Topič, and F. Smole, "A detailed study of monolithic contacts and electrical losses in a large-area thin-film module," *Progr. Photovoltaic Res. Appl.*, vol. 13, no. 4, pp. 297–310, 2005.

[15] G. T. Koishiyev, "Analysis of impact of non-uniformities on thin-film solar cells and modules with 2-D simulations," Ph.D. dissertation, Dept. Phys., Colorado State Univ., Fort Collins, USA, 2010.

[16] H. Hoppe, M. Seeland, and B. Muhsin. (2011). "Optimal geometric design of monolithic thin-film solar modules: Architecture of polymer solar cells," *Solar Energ. Mater. Solar Cells* [Online]. Available: http://www.sciencedirect.com/science/article/pii/S092702481100523X

[17] B. E. Pieters, "Spatial modeling of thin-film solar modules using the network simulation method and spice," *IEEE J. Photovoltaic*, vol. 1, no. 1, pp. 93–98, Jul. 2011.

[18] P. Maffezzoni and D. D'Amore, "Compact electrothermal macromodeling of photovoltaic modules," *IEEE Trans. Circuits Syst. II: Exp. Briefs*, vol. 56, no. 2, pp. 162–166, Feb. 2009.

[19] D. Shvydka and V. G. Karpov, "Power generation in random diode arrays," *Phys. Rev. B*, vol. 71, pp. 115314-1–115314-5, Mar. 2005.

[20] D. Shvydka, J. P. Rakotoniaina, and O. Breitenstein, "Lock-in thermography and nonuniformity modeling of thin-film CdTe solar cells," *Appl. Phys. Lett.*, vol. 84, no. 5, pp. 729–731, 2004.

[21] U. Malm and M. Edoff, "Influence from front contact sheet resistance on extracted diode parameters in CIGS solar cells," *Progr. Photovoltaic Res. Appl.*, vol. 16, no. 2, pp. 113–121, 2008.

[22] S. Vergura, G. Acciani, and O. Falcone, "Modeling defects of PV-cells by means of FEM," in *Proc. Int. Conf. Clean Electr. Power*, Jun. 2009, pp. 52–56.

[23] O. Breitenstein, W. Warta, and M. Langenkamp, *Lock-in Thermograph* (ser. Springer Series in Advanced Microelectronics), vol. 10. Berlin, Germany: Springer-Verlag, 2010.

[24] M. Langenkamp and O. Breitenstein, "Classification of shunting mechanisms in crystalline silicon solar cells," *Solar Energ. Mater. Solar Cells*, vol. 72, no. 1–4, pp. 433–440, Apr. 2002.

[25] O. Breitenstein, "Nondestructive local analysis of current–voltage characteristics of solar cells by lock-in thermography," *Solar Energ. Mater. Solar Cells*, vol. 95, no. 10, pp. 2933–2936, 2011.

[26] V. G. Karpov, "Coupled electron-heat transport in nonuniform thin film semiconductor structures," *Phys. Rev. B*, vol. 86, pp. 165317-1–165317-11, Oct. 2012.

[27] G. Sartoris, "A 3D rectangular mixed finite element method to solve the stationary semiconductor equations," *SIAM J. Sci. Comput.*, vol. 19, no. 2, pp. 387–403, 1998.

[28] Institute of Computational Physics, Zurich University of Applied Sciences, Winterthur, Switzerland, NM-SESES Manual. (2012). [Online]. Available: http://www.icp.zhaw.ch/engineering/icp/software/nm-seses.html

[29] J. O. Schumacher, J. Eller, and G. Sartoris. "A 2+1D model of a proton exchange membrane fuel cell with glassy-carbon micro-structures," *Proc. MATHMOD.*, 2009.

[30] M. A. Green, *Solar Cells: Operating Principles, Technology, and System Applications*. Englewood Cliffs, NJ, USA: Prentice–Hall, 1982.

Thomas Lanz (M'12) was born in Bern, Switzerland, in 1983. He received the M.Sc. degree in physics from ETH Zurich, Zurich, Switzerland, in 2009. He is currently working toward the Doctoral degree in photonics at the Ecole Polytechnique Fédérale de Lausanne, Lausanne, Switzerland.

He is also a Research Assistant at the Zurich University of Applied Sciences Winterthur, Switzerland. Previously, he was a Research Assistant with ETH Zurich, for electrochemical impedance spectroscopy and macroeconomics. His research interests include numerical electromagnetics for renewable energy applications and computational engineering for optoelectronic device characterization.

Mathias Bonmarin (M'12) was born in Bern, Switzerland, in 1979. He received the Dipl.Ing. degree in biomedical engineering from the Polytechnic University of Marseille, Marseille, France, in 2002, and the Ph.D. degree in physics from the University of Zurich, Zurich, Switzerland, in 2010.

He is currently a Research Associate at the Zurich University of Applied Sciences, Winterthur, Switzerland. His research interests include passive and active thermal imaging for the nondestructive testing of materials.

Michael Stuckelberger was born in Zurich, Switzerland, in 1982. He received the diploma in Physics from ETH Zurich, Zurich, Switzerland, in 2009. He is currently working toward the Ph.D. degree in material science at the Ecole Polytechnique Fédérale de Lausanne (EPFL), Neuchâtel, Switzerland.

He is also a Research Assistant at EPFL. His current research interests include amorphous silicon materials with tunable properties and their applications in thin-film silicon solar cells.

Christian Schlumpf was born in Montreal, QC, Canada, in 1988. He received the B.Sc. degree in engineering physics from Queen's University, Kingston, ON, Canada, in 2011.

He is currently a Research Engineer at the Ecole Polytechnique Fédérale de Lausanne, Neuchâtel, Switzerland. Previously, he was a Summer Engineer with consulting firms Hatch Associates, and AMEC Nuclear Safety Solutions. His current research interests include photovoltaic module design, reliability, and testing.

Christophe Ballif received the Graduate degree in physics and the Ph.D. degree in novel PV materials from the Ecole Polytechnique Fédérale de Lausanne (EPFL), Neuchâtel, Switzerland, in 1994 and 1998, respectively.

He accomplished the Postdoctoral Research at NREL, Golden, CO, USA. He then worked at the Fraunhofer ISE, Freiburg, Germany, on crystalline silicon until 2003, and then at the EMPA, Thun, Switzerland, before becoming a full Professor at the Institute of Microtechnology (IMT), University of Neuchâtel, Neuchâtel, in 2004, taking over the chair of Prof. A. Shah. Since 2009, he has been the Director of the Photovoltaics Laboratory at the IMT Neuchâtel, part of the EPFL. With close to 60 employees in 2012, this laboratory contributes to technology transfer and industrialization of novel devices, processes and equipments with numerous companies active in the solar field.

Beat Ruhstaller was born in Einsiedeln, Switzerland, in 1972. He received the Diploma in physics from ETH Zurich, Zurich, Switzerland, and the Ph.D. degree from the University of California, Santa Cruz, USA.

He was involved in OLED modeling at the IBM Almaden Research Center, San Jose, CA, USA, as well as in OLED display technology development at the IBM Zurich Research Laboratory, Rüschlikon, Switzerland. As a Professor at the Institute of Computational Physics, Zurich University of Applied Sciences, Winterthur, Switzerland, he is heading a research group on modeling and characterization of organic electronics and photovoltaics. He is founder of the spin-off company Fluxim AG that commercializes simulation software for OLED displays and lighting as well as photovoltaics.